Mechanical and optical degradation of flexible optical solar reflectors during simulated low earth orbit thermal cycling

B. Putz[1,2], S. Wurster[1], T.E.J. Edwards[2], B. Völker[4+], G. Milassin[5], D.M. Többens[6], C.O.A. Semprimoschnig[5], M.J. Cordill[1,3]

[1] Erich Schmid Institute of Materials Science, Austrian Academy of Sciences, Leoben, Austria

[2] Empa, Swiss Federal Laboratories for Materials Science and Technology, Thun, Switzerland

[3] Dept. of Materials Science, Montanuniversität Leoben, Leoben, Austria

[4] Max-Planck-Institut für Eisenforschung, Düsseldorf, Germany

[5] European Space Research and Technology Centre (ESTEC), Noordwijk, The Netherlands

[6] Helmholtz-Zentrum Berlin für Materialien und Energie, Albert-Einstein-Str. 15, 12489 Berlin, Germany
[+] Now at: Materials Center Leoben Forschung GmbH, Roseggerstraße 12, 8700 Leoben, Austria

*corresponding author: barbara.putz@empa.ch, +41 587 656 254

Abstract

Multilayer thin film systems on flexible polymer substrates are used as flexible optical solar reflectors or thermal insulation of satellites and spacecraft. During one year of operation, a satellite in low earth orbit typically encounters 6000 thermal cycles of ± 100°C. Due to the different coefficients of thermal expansion between the individual layers and the substrate it is important to investigate the thermo-mechanical stability of the multilayers as a function of the cyclic heat load. Scanning electron microscopy and focused ion beam cross-sectioning revealed that Inconel-Ag bilayers on fluorinated ethylene propylene (FEP) substrate severely degrade during thermal cycling of ± 150°C in a gaseous N_2 atmosphere. After only 100 cycles through thickness cracks and subsurface voids in the Ag layer form as a result of equi-biaxial thermal stresses caused by the large difference in thermal expansion between film and substrate. Transmission Kikuchi Diffraction (TKD) before and after thermal cycling also revealed grain growth and twin widening in the Ag layer. Cracking and void formation are detrimental to application relevant material properties including corrosion protection (Inconel) and reflectivity (Ag). Reflectance measurements revealed that the amount of reflected energy as well as the reflection mode (specular vs. diffuse) significantly change during the first 100 cycles. Saturation of reflection characteristics was observed after 25 cycles, which correlates to a turning point in the evolution of Ag voids. Results of this study indicate that special focus should be directed towards thermal stress control ($\Delta\alpha$) and tailoring of the metal-polymer interface to improve resistance of versatile metal-polymer systems against thermal cycling.

1. Introduction

Thin films on polymer substrates are a highly attractive field of research with applications ranging from ordinary food packaging [1] to flexible electronics [2,3] or advanced insulation devices. High-end applications include flexible optical solar reflectors (OSRs) for passive thermal control of satellites and spacecraft in orbit. Typically, such flexible systems are also referred to as second surface mirrors (SSMs) while the term OSR was historically introduced for quartz glass with a metallic backside coating. In principle, the applications for both are identical, but satellites increasing in size triggered the replacement of glass in conventional rigid OSRs by transparent polymer substrates, bringing along weight savings, reduced launch costs, structural flexibility and facilitated assembly. The combination of a highly reflective metal layer on a transparent substrate allows engineering of unique thermo-optical properties. Incoming solar radiation (short wavelengths, λ) is reflected at the metal layer, while internally generated heat (wavelengths in the infrared region) is radiatively dissipated via the polymer substrate resulting in a low solar absorptance, α, and a high infrared (IR) emittance, ε. A detailed description of the OSR principle can be found in [4]. Ag thin films (150 nm) and fluorinated ethylene propylene (FEP, Teflon®), investigated in this study, are a typical combination for flexible OSRs for the high reflectivity and the high transparency/IR-emittance, respectively. Additionally, a thin Inconel overcoat (27.5 nm) on top of Ag assures corrosion protection. Regarding reflectivity, a directional specular reflection mode, typical for very smooth surface, is required. In contrast to undirected diffuse reflection it allows one to accurately predict and model the temperature distributions onboard a satellite.

During the life cycle of a satellite (up to 15 years for telecommunication [5]) the flexible OSR must withstand the harsh space environment, as well as extreme thermal cycling during orbit. Extended exposure to UV radiation or atomic oxygen are known to alter material properties [6], causing embrittlement and opaqueness of polymers and posing reliability issues to missions after 3-5 years [5]. For FEP foils, increased crystallinity, surface cross-linking or chain scission have been observed in the top surface layer in ground tested and space-retrieved samples depending on the type of exposure [7]. Surface changes were related to shifts in the polymer's local melting temperature T_m. Less is known about the influence of thermal cycling on thermo-optical, mechanical and electrical properties of flexible OSRs as a whole, as well as other metal-polymer composites for similar applications. In low earth orbit (LEO), temperatures typically range between ± 100°C [8,9] with 16 thermal cycles per day [10]. In flexible electronics thermal cycling also

occurs, caused by current induced heating and on/off switching of domains. Due to the large difference in thermal expansion coefficients between film and substrate (α_{FEP} = 127 ppm/K [11], α_{Ag} = 20 ppm/K [12]) the generation of thermal stresses can cause changes to the film, the substrate or the interface, often the weakest link in the system. Phenomena such as cracking [9], thermo-mechanical fatigue and surface roughening [13–17] or stress migration [18,19] and micro-voiding [18] have been reported, predominantly on rigid substrates. Regarding interfacial stability, systems with thin amorphous interlayers between the film and the substrate have been found to be extremely stable and resistant to thermal cycling [20,21].

In this work we report the thermo-mechanical stability of the Inconel/Ag/FEP system as a function of thermal cycling following simulated LEO conditions. Severe material degradation, including crack formation and sub-surface voiding at the Ag-FEP interface at low cycle numbers, results in decreased reflectivity and an unfavorable change in the reflection mode. The large $\Delta\alpha_{th,FEP-Ag}$ combined with the weak Ag-FEP interface are the main reasons for the poor thermo-mechanical performance. The results highlight the importance and potential of composite design and interfacial engineering in order to develop strong and thermally stable metal-polymer systems for flexible OSRs and various other terrestrial flexible thin films applications.

2. Experimental

Evaporated Ag films (nominal thickness 150 nm) on a 50 μm FEP substrate were supplied by Sheldahl Brand. To protect the Ag film from terrestrial corrosion, a 27.5 nm overcoat of Inconel was applied.

Thermal cycling (0-100 cycles) was performed with a Weiss Enet Temperature Chest Facility in a gaseous N_2 environment. A4 sized sheets of coated FEP were fixed to the base plate of the furnace with Al-tape at the corners to ensure good thermal contact. Samples for subsequent characterisation were taken far enough from the fixation points to avoid distortion of the results. The maximum and minimum temperature for one thermal cycle were ± 150°C with a heating rate of 10°C per minute. At the maximum and minimum temperatures a hold period of 15 min was applied.

After thermal cycling, the Inconel surface was investigated with scanning electron microscopy (SEM, LEO 1525, operation voltage: 2 kV and 15 kV). Imaging at 15 kV allowed the observation of voids in the buried Ag layer (Figure 1). For the as-deposited film system images of

the same Inconel surface at 2 kV and 15 kV (Figure 1a,b) show that variations in the acceleration voltage do not significantly alter the appearance of the surface. Prominent surface features are highlighted with white circles to facilitate comparison. After 100 thermal cycles of ± 150°C imaging of the same area at 2 kV (Figure 1c) and 15 kV (Figure 1d) acceleration voltages allows the observation of subsurface voids in the buried Ag layer. The voids are visible as black spots only in the 15 kV image. In Figure 1c "ridges" (arrows) are observed on the Inconel surface and are areas where the film is higher than the rest of the surface. Often the ridges correlate to locations where voids are found (see Figure 1d).

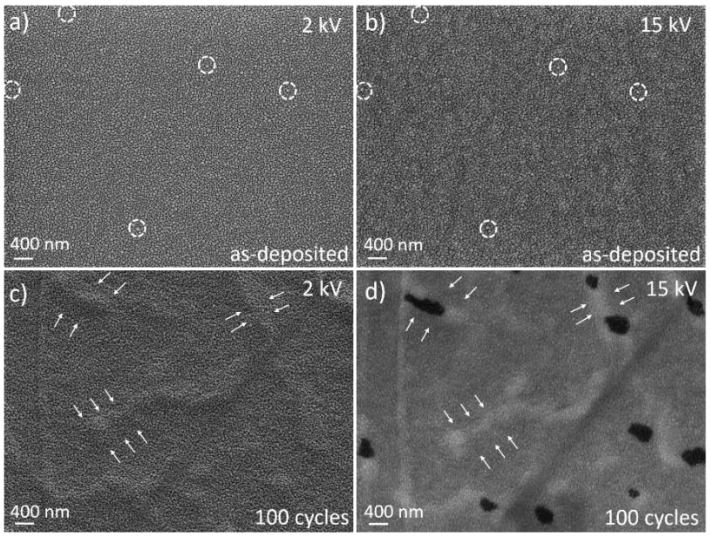

Figure 1: Investigation of thermally induced, subsurface Ag voids with SEM using specific imaging conditions. (a) 2 kV and (b) 15 kV SEM images of the same Inconel surface demonstrating that for the as-deposited film system, variations in the acceleration voltage do not significantly alter the appearance of the surface. Prominent surface features are highlighted with white circles for comparison. After 100 thermal cycles of ± 150°C imaging of the same area at (c) 2 kV and (d) 15 kV acceleration voltage allows to identify the position of subsurface voids in the underlying Ag layer, visible as black spots only in the 15 kV image. Arrows in (c) and (d) indicate "ridges" that form during thermal cycling.

Following the approach described in [20], SEM images were analysed with ImageJ [22] to quantify the amount of voids in the Ag film due to the thermal cycling. Original 15 kV SEM images (Figure 2a) were converted to binary images using a constant threshold to separate the voids in the Ag layer (white) from the surface (black). The black and white images were further used to analyse void quantity and size with the 'analyze particle' tool as a function of thermal cycling (Figure 2b, voids outlined with black lines). Four images of the same magnification (image size: 45.4 μm^2)

were analysed for each cycle number and a mean value with standard deviation was determined. Finally, cross-sectional focused ion beam cuts (FIB, Zeiss AURIGA crossbeam, operation voltage: 30 kV, operation currents: 500 pA coarse-cut, 50 pA polishing, operation voltage SEM: 5 kV) were used to identify the voids in the Ag layer.

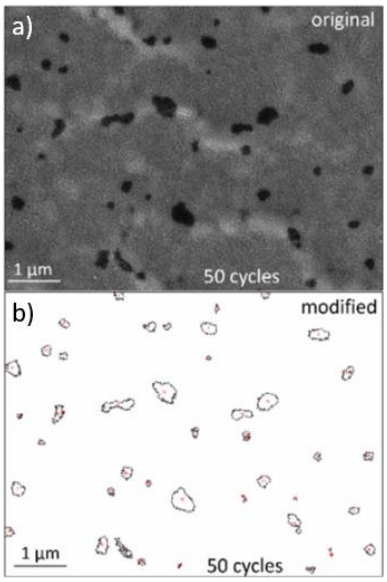

Figure 2: Evaluation of voids in the Ag layer as a function of thermal cycling. Example of an original 15 kV SEM image (a) and after processing (b) used to quantify the number and size of voids. The outlines of the voids are drawn in black in the processed image.

The microstructure of the Ag layer was characterised with Transmission Kikuchi Diffraction (TKD) [23]. TKD samples were prepared in two different ways: i) For the as-deposited material the Ag/Inconel bi-layer was peeled off from the FEP substrate and floated onto a Cu grid. Subsequently, a short Ar^+ ion milling in a Gatan precision ion polishing system (PIPS II, model 695) with liquid N_2 cooling was performed from the Ag side to further thin the sample and remove polymer residues. Due to severe cracking of the thin film during thermal cycling this peel-approach was not suitable for cycled samples. ii) A focus ion beam (FIB, Helios NanoLab Dualbeam) lift out method for transmission electron microscopy lamellae was adapted to fabricate TKD samples after thermal cycling. The fabrication process is schematically shown in Figure 3. For FIB processing small pieces (2 x 3 mm) were cut with a scalpel. In a first step, the region damaged from the cutting (~50 µm) was removed along the top edge (Cutting step 1, Fig. 3a, voltage 30 kV, current 10.3 nA,). Subsequently, the majority of the polymer substrate was removed by cutting into the cross-section in a selected area of interest (Cutting step 2, Fig. 3b, 10.3 nA coarse cutting,

0.2 nA fine cutting towards the thin film), leaving a thin layer of polymer on the backside of the lamella. The lamella was cut out (Cutting step 3, Fig. 3b and 3c, current 80 pA) and lifted onto a TKD Cu grid, fixing it with Pt on two corners (Fig. 3d). In a final thinning step, the remaining polymer on the backside was removed (2 kV, 40 pA, incident angle 7°). During sample preparation, FIB exposure of the Inconel surface was carefully avoided. The final lamella (Fig. 3d) contains an area with voids (left) and without voids (right, close to a thermal crack).

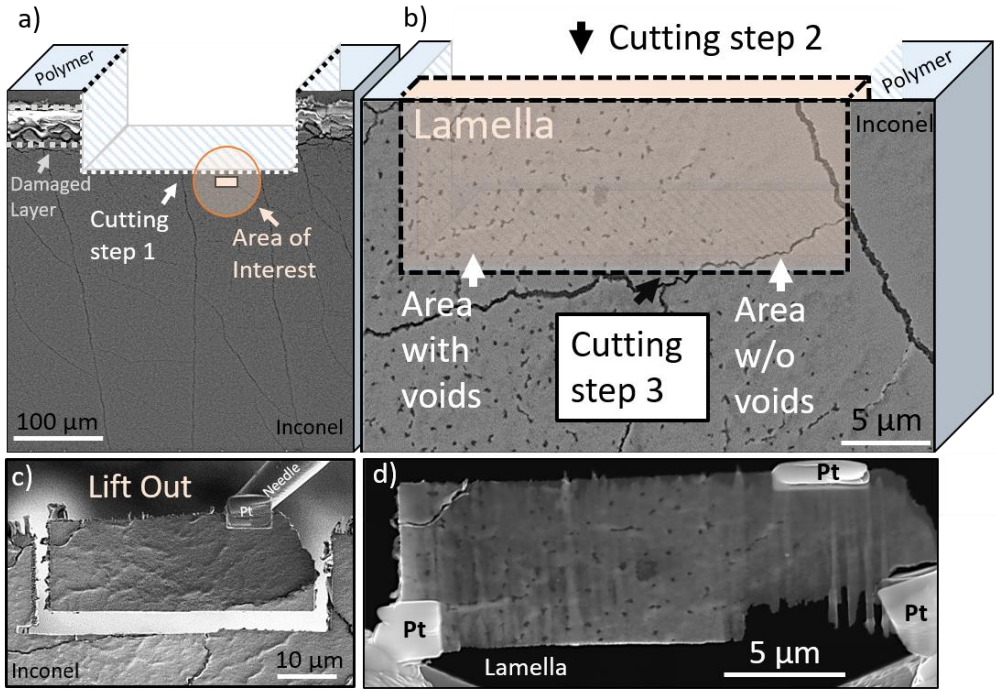

Figure 3: FIB preparation of the TKD lamella for thermally cycled material. Schematics of the necessary cutting steps (1-3) to a) remove the damaged edge layer and b) lift out the lamella. c) SEM image of the lift out process. d) Final lamella mounted on a Cu grid on two corners with Pt. The lamella contains two areas as indicated in b): with voids (left) and without voids (right, close to a thermal crack).

TKD measurements of the Ag microstructure (30 kV, working distance: 3 mm, step size: 12 nm – as-deposited / 10 nm - 100 thermal cycles) were performed through the bilayer from the Inconel side, as the TKD signal originates only from the bottom 10 nm of the sample [24]. Data processing was done with the OIM Analysis^{TM} software. Parameters for grain size analysis include a single iteration grain dilation clean-up procedure, a maximum misorientation angle of 5° for grain boundary definition and a minimum number of 5 pixel per grain. In all cases a minimum of 500 grains were measured conforming to the ASTM standard E2627-13. One should note that due to the TKD scan size it was not possible to exceed the 100 point-counts/grain limit specified in

E2627-13. The film thickness of the Inconel layer is in the few tenth of nm (27.5 nm), which standardly results in a grain size in the order of the film thickness [25,26].

XRD analysis (synchrotron radiation, KMC-2 beamline [27], BESSY II, Berlin) was used to investigate the residual lattice strains in the Ag film as a function of thermal cycling. A Bruker VÅNTEC 2000 area detector, exposure times of 5 s and a beam wavelength of 0.154 nm were employed. Residual lattice strains were measured with the $\sin^2\psi$ method [28]. The 111 and 200 Bragg peaks of the Ag layer were recorded in reflection geometry using 10 different ψ angles between 0 and 45 degrees. A Pearson fit was applied to determine peak positions and peak widths. Film stresses were calculated using X-ray elastic constants (XECs) (1/2 S2) [29] for untextured 111 and 200 Ag reflections. XECs were calculated from single-crystal elastic constants assuming the Hill model with the software ElastiX [30]. The Inconel overcoat was too thin to receive a sufficient signal for $\sin^2\psi$ analysis.

Reflectivity measurements were performed using an Agilent Cary 5000 spectrometer with an external integration sphere accessory. The total and the diffuse solar reflectance were measured separately as a function of thermal cycling on circular areas with a diameter of 16 mm.

3. Results

3.1 Surface morphology

Thermal cycling caused significant degradation of the metallisation. In Figure 4 representative SEM images of the Inconel film surface are shown as a function of thermal cycling at two different magnifications using 15 kV operating voltage. In the as-deposited state (0 cycles) the surface is very smooth and void free. After 3 cycles the first thermal cracks which penetrate both metal layers are visible (inserts). It is known that the cracks are through both layers because the film system was examined through the transparent FEP substrate and the same cracks were observed in the Ag film as from the Inconel film on the top surface. Through thickness crack formation can only be caused by thermal stresses resulting from the different expansion coefficient of the polymer substrate ($\alpha_{FEP} = 127 \cdot 10^{-6}$ K^{-1} [11]) and the metal films ($\alpha_{Ag} = 20 \cdot 10^{-6}$ K^{-1} [12], $\alpha_{Inc} = 13 \cdot 10^{-6}$ K^{-1} [31]). In addition to thermal cracking, a second degradation mechanism, namely the formation of subsurface voids in the Ag layer, was observed as black spots using certain SEM imaging conditions (Figure 1 and 4). Small black spots were first visible after 6 thermal cycles. With increasing cycle number, the size and density of the black spots increases. Voids form near or under ridges in the Inconel layer, which are similar to spontaneous buckles or wrinkles [32,33]

which form due a compressive residual stress. Up to 12 cycles the ridges are generally intact on the surface, at and above 25 cycles many ridges crack at the apex.

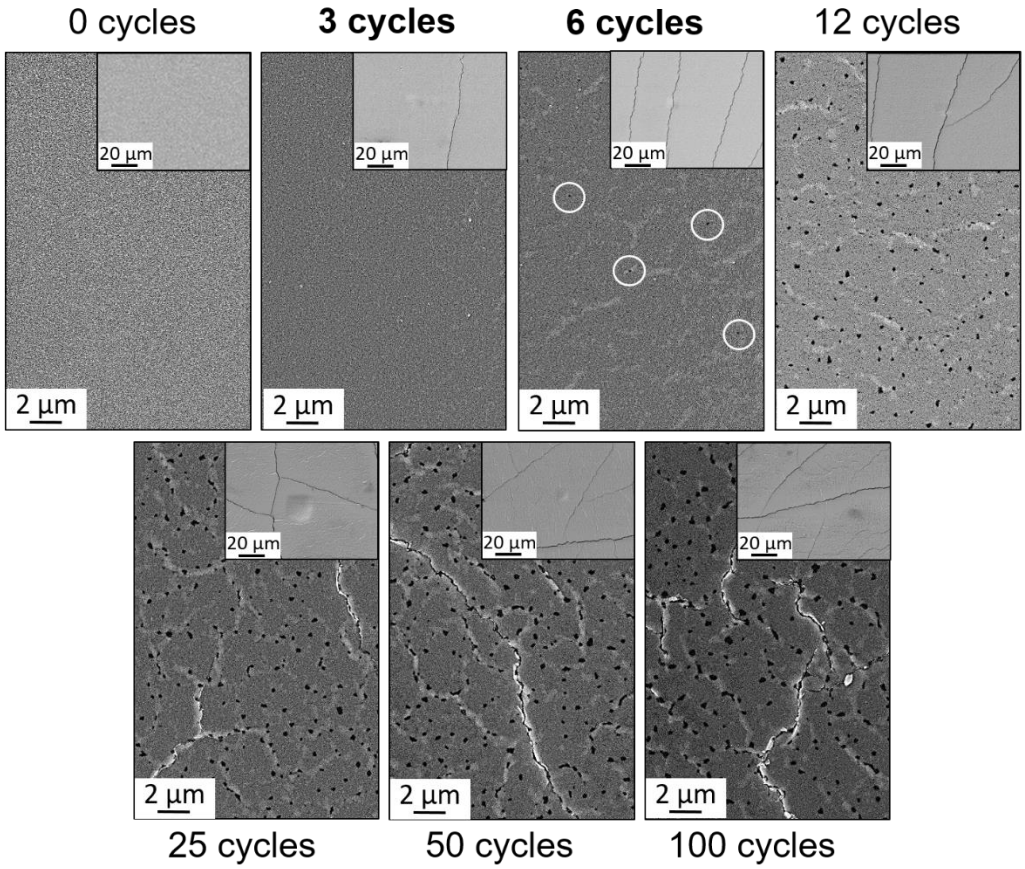

Figure 4: SEM overview (inserts) and higher magnification images showing the evolution of the film damage as a function of thermal cycling. Thermal cracks are visible after 3 cycles (insert). Voids in the underlying Ag layer are visible after 6 cycles (white circles). All images were recorded using the same imaging conditions (15 kV operating voltage).

The overview image in Figure 5a shows that the void distribution is inhomogeneous and locally restricted. Subsurface voids only form a certain distance away from the initially formed thermal through thickness cracks, indicating that stress driven diffusion of Ag is responsible for void formation. As soon as the thermal stresses exceed the fracture stress of the thin film system, the thermal cracks form and a local relaxation of film stresses along the crack edges occurs. In the vicinity of cracks, the film stress gradually increases as a function of shear stress supported by the interface [34,35]. The mean distance between thermal cracks and first Ag voids was measured as 7.4 ± 1.6 µm from SEM images for all cycles. X-ray diffraction experiments are a common way to measure strains/stresses in flexible thin films. Measurement of the local stress distribution between

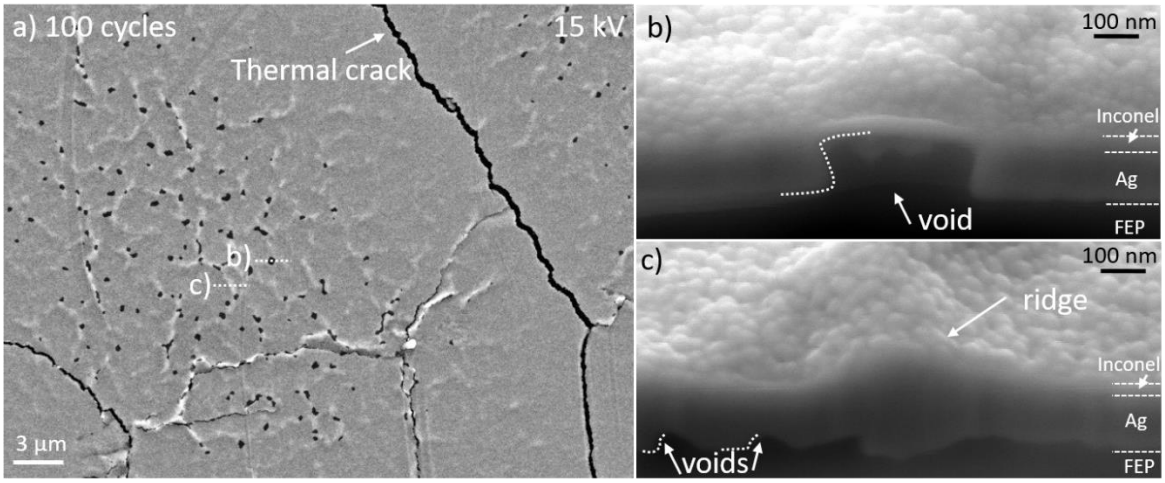

Figure 5: Thermally induced degradation of FEP-Ag-Inconel after 100 thermal cycles of ± 150°C in gaseous N_2. (a) On the Inconel surface pronounced through thickness cracks and areas containing black spots are visible. Cross-sectional view on (b) a through thickness void in the underlying Ag layer and (c) a ridge without substantial voiding. Representative positions of the FIB cuts are indicated in (a).

fragments with high spatial resolution at exact distances away from thermal cracks has not been performed yet. Possible methods to resolve stresses locally could be high resolution EBSD [36] or in situ Raman spectroscopy [37]. Figure 5b and 5c show representative FIB cross-sections of a through thickness void and an uncracked ridge, respectively. Representative positions of the cuts are indicated in the overview image (Figure 5a). The Inconel layer above the Ag void (Figure 5b) remains intact. There is no change in Inconel film thickness compared to the regions surrounding the void. Below the Inconel ridge (Figure 5c) there is a local increase of the Ag film thickness, indicating the accumulation of material in ridge-regions. In the vicinity of the ridge, small voids are visible at the FEP-Ag interface. The diffusion of the Ag atoms and vacancies to create the voids is also responsible for the creation of the ridges.

To investigate the evolution of Ag voids in the film thickness direction, FIB cuts were performed through the voids after different numbers of thermal cycling. Figure 6 shows a cross-sectional view of voids after 50 cycles. A strong reaction of the FEP substrates with the electron beam exacerbates cross-sectional imaging and analysis. As shown in Figure 6 void formation typically starts at the Ag-FEP interface and the voids progressively grow through the film thickness. After 50 cycles not all voids penetrate the Ag layer completely, as illustrated in Figure 6. In addition to void evolution, FIB cuts revealed a columnar grain structure of the Ag layer.

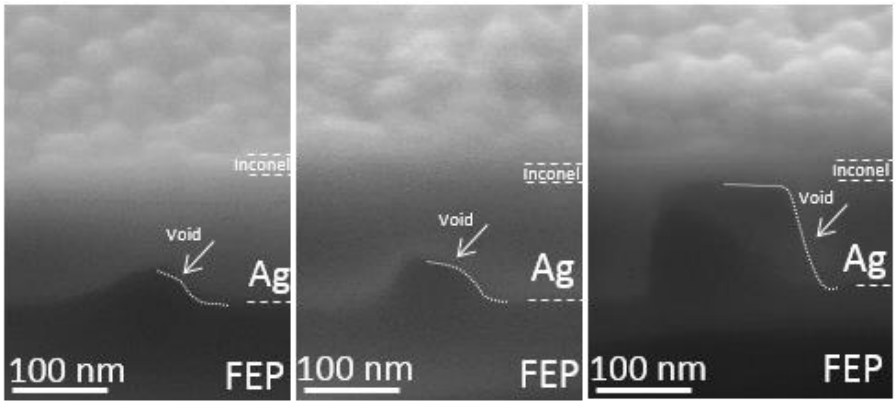

Figure 6: Cross-sectional analysis of void formation after 50 thermal cycles. Voids start to form at the Ag-FEP interface and grow through the Ag layer. Interfaces as well as voids are indicated with white lines.

The SEM images at 15 kV were used to analyse the formation and lateral growth of the voids in the Ag layer as function of thermal cycling. From the processed images the average number of voids per area and the average size of the voids were measured. Figure 7 summarizes the results of the analysis as a function of thermal cycling. Voids are first observed after 6 thermal cycles. At this early stage only a few small voids are present (approximately 0.1 voids/μm^2). After initial void formation, the number and size of the voids increases with increasing cycle number. After 25 thermal cycles no further voids are nucleated and the number of voids per area saturates, indicated by the plateau in the blue dashed curve (average 0.9 voids/μm^2). While void nucleation has stopped, film damage is still progressing as present voids continue to grow, indicated by the increasing void area (illustrated by the black line in Figure 7a). The average area of a single void after 100 thermal cycles was measured as 0.044 ± 0.011 μm^2.

To facilitate comparison between the film microstructure and the size of voids, a mean diameter of the voids was calculated from the average measured void area, assuming circular void shapes. Figure 7b summarizes void diameter as a function of thermal cycling, including the standard deviation calculated following the rules of propagation of uncertainty. Results indicate that the size of the voids is of the order of the initial Ag microstructure. After 12 cycles the void diameter is similar to the smaller grains in the initial in-plane Ag grain size distribution (columnar grains, average in-plane grain size: 255 ± 136 nm, excluding twins as grain boundaries), indicating that at this early stage already Ag grains are lost. After 100 cycles the average void diameter increases to about 240 nm.

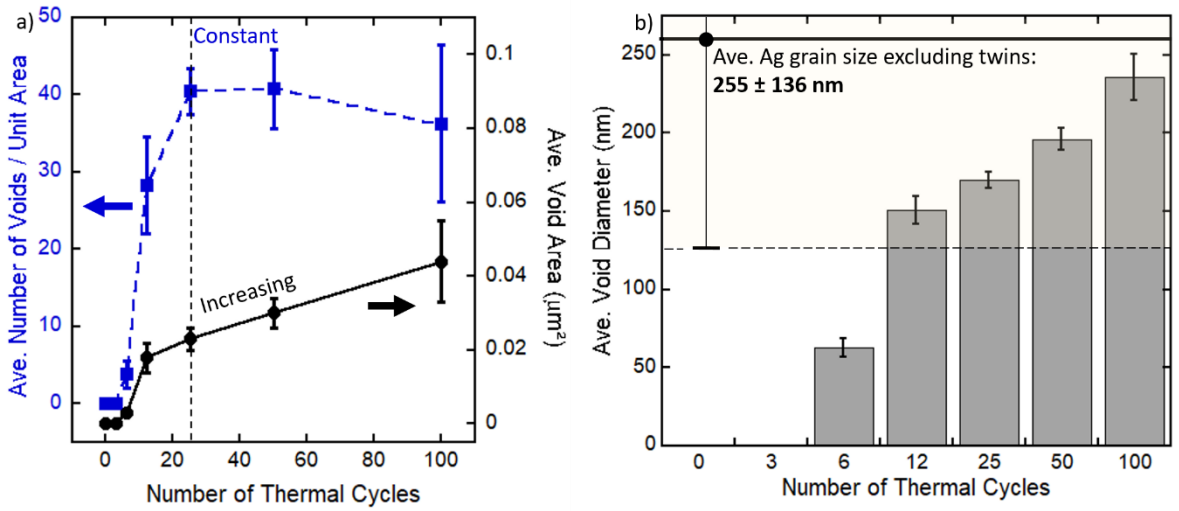

Figure 7: Statistical analyses of void evolution in the Ag layer. (a) Average number of voids per area (blue squares) and average void area (black circles) as a function of thermal cycling. While the number of voids saturates after 25 cycles, the average size of individual voids continues to increase, indicating progressive film damage. The lines are only used to guide the eye. (b) Comparison of the average void diameter with the average Ag grain size excluding twins, illustrating that the voids grow larger than the smaller grains in the initial in-plane grain size distribution.

3.2 TKD analysis

FIB cross-sections revealed a columnar grain structure of the Ag layer in the thickness direction. The in-plane microstructure of the Ag layer was investigated with TKD as a function of thermal cycling. The TKD results are summarized in Figure 8. Due to the inhomogeneous spatial distribution of the voids after thermal cycling, TKD maps were collected from regions with a high void density (A) and from regions close to a thermal crack (B), where no voids are present. The two regions (A & B) are indicated in the small SEM image in Figure 8. Figure 8a shows representative out of plane crystal orientation (IPFz) maps of the Ag layer in the as-deposited state and after 100 thermal cycles. Black spots in the TKD map of region A after cycling correspond to voids in the Ag layer. In Figure 8b, the Ag grain size distributions based on the area fraction are shown for the three different cases. For grain size analysis, twins were identified and excluded as grain boundaries. The minimum grain size was defined as 20 nm, based on the TKD step size (10-12 nm) and the cut-off grain size of 5 pixel^2. In the as-deposited state, the average grain size is 255 ± 136 nm with a maximum cut-off grain size of around 500 nm. After 100 thermal cycles an increase is observed in the average grain size (300 ± 150 nm) as well as the maximum cut-off grain

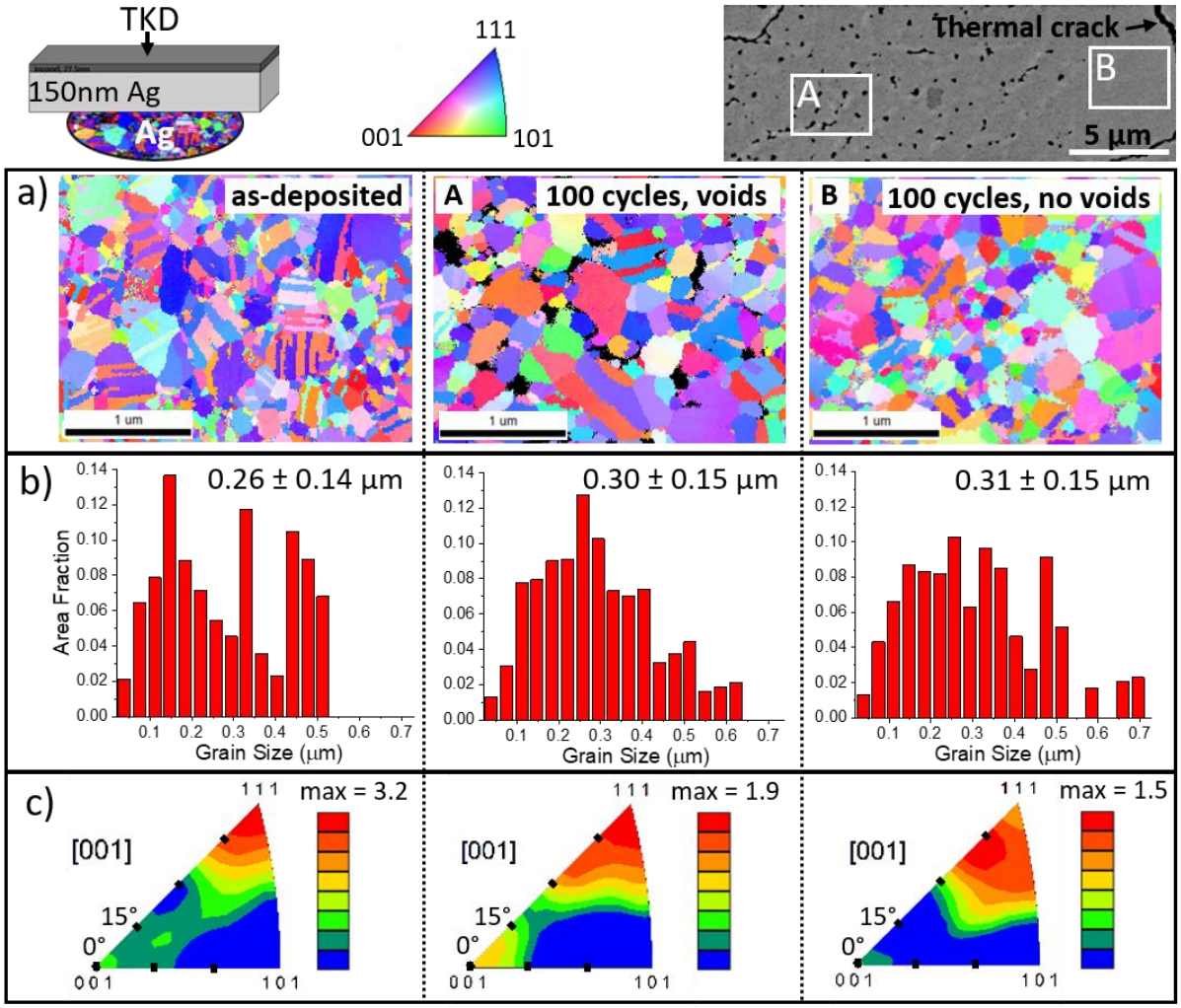

Figure 8: TKD analysis of the Ag microstructure. a) Representative out of plane crystal orientation (IPFz) maps of the Ag layer in the as-deposited state and after 100 thermal cycles. Due to the spatial distribution of voids, IPFz maps after cycling are collected from regions with a high void density and regions with no voids. The different regions are indicated with white rectangles in the SEM image above. Additionally, a schematic of the TKD setup on the Inconel-Ag bilayer system is included at the top. b) Ag grain size distribution based on the area fraction in different regions before and after 100 thermal cycles. Average grain size values are included. c) Corresponding inverse pole figures indicating a slight (111) texture of Ag in the out of plane direction.

size. There is no significant difference in the average grain size between region A and B. Grain growth due to thermal cycling has been observed by several studies [14,15]. Figure 8c shows inverse pole figures (IPFs) corresponding to the out of plane crystal orientation maps. Generally, the Ag layer exhibits a slight (111) texture in the out of plane direction. Besides a small decrease in texture, no significant change is observed after 100 thermal cycles. The small shift of the

maximum in the IPF away from the (111) pole after cycling is most likely due to the FIB preparation method, as local bending along the length of the thinned lamella can result in a tilt of the surface relative to the defined sample coordinate system.

3.3 XRD analysis

Stress measurements of the Ag layer revealed that compressive stresses accumulate in the Ag film with increased cycling. The evolution of the residual stresses as a function of thermal cycling is summarized in Figure 9. It should be noted that the results derived from the Ag 111 and 200 reflections follow the same trend, affirming good quality of the XRD analysis. In the as-deposited state, a small amount of residual tensile stress is present in the Ag layer. Upon thermal cycling compressive stresses build up, reaching a maximum at 12 thermal cycles. After the peak, compressive stresses are relaxed resulting in a stress free plateau for the intermediate cycle numbers. Following the plateau, a second increase in compressive stress is observed between 50 – 100 thermal cycles. The rate of stress increase at high cycle numbers is lower compared to the rapid increase below 12 cycles, most likely indicating changed conditions in the Ag layer.

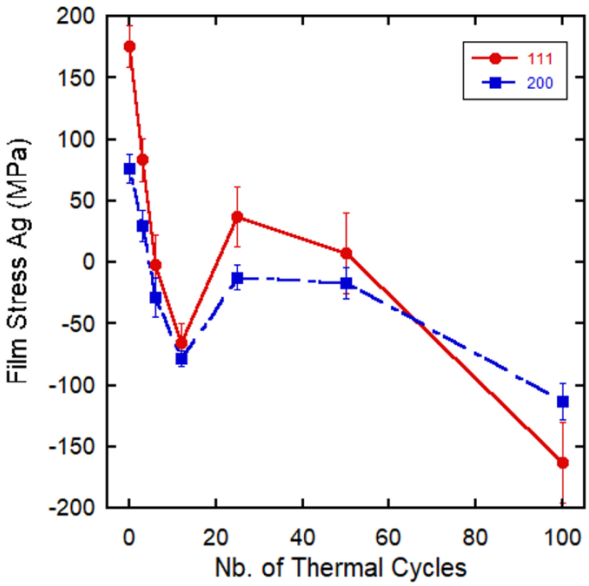

Figure 9: Evolution of residual stresses in the Ag layer as a function of thermal cycling derived from 111 and 200 reflections. With increasing cycle number compressive stresses build up in the Ag layer as a result of material redistribution during void formation.

3.4 Reflectivity

To investigate the influence of thermal cracking and voiding on application relevant material properties, solar reflectance was measured as a function of thermal cycling. The measured values represent the reflected fraction of incoming radiation at near normal incidence with the air mass zero solar spectrum (AM0). The used wavelength range of 250 – 2500 nm covers approximately 97% of the AM0 spectrum (ASTM E490). The total solar reflectance, ρ_T, and the diffuse solar reflectance, ρ_D, were measured independently. By subtracting the diffuse from the total reflectance the specular reflectance, ρ_S, was calculated following the equation: $\rho_S = \rho_T - \rho_D$. Specular reflection, where the incidence angle is equal to the angle of reflection, is typical for smooth surfaces. For diffuse reflection, generated by a rough surfaces, the incidence angle gives rise to a multiplicity of reflection angles. Following the in-use conditions of the material as a solar reflector, measurements were conducted from the transparent FEP side. The obtained values represent the reflection characteristics of the Ag layer. As a result of the experimental setup potential changes in the polymer substrates due to thermal cycling are also included in the obtained reflectivity values, as the light passes through the FEP substrate twice during the measurement. In partly crystalline polymers the fraction of crystallinity can change over time as a result of thermal aging [38] or space exposure [9]. Changes in the polymer crystallinity typically result in a change of color, such as from transparent towards opaque. Visual inspection of the FEP substrate after cycling did not reveal any observable sign of color change. After 100 thermal cycles the substrate appears as transparent as in the initial state, indicating that there is no significant influence of the polymer on the reflectivity measurements. These findings are in line with the results of thermally cycled Al films on FEP reported in [9], showing that thermal cycling seems not to directly affect the properties of the polymer. The dielectric behavior of the polymer substrate determines the emittance of flexible OSRs. The values of normal and hemispherical emittance ε_N and ε_H for pristine Ag/Inconel-coated 50 µm FEP substrate are ≥ 0.60 [39]. As the thickness of FEP does not change within the applied cycle number also the emittance will likely remain unaffected, as has previously been reported [8–10]. The results of the performed reflectivity measurements, including absolute and relative values for ρ_T, ρ_D and ρ_S are summarized in Table 1 and Figure 10. All three parameters indicate a deterioration of reflective properties resulting from the degradation of the Ag layer with thermal cycling.

Table 1: Summary of reflectivity measurements as a function of thermal cycling.

FEP side (Ag)	**Solar Reflectance, ρ**		
Thermal cycles	Total (ρ_T)	Diffuse (ρ_D)	Specular ($\rho_S = \rho_T - \rho_D$)
as-deposited, 0	0.94	0.04 (4%)	0.90 (96%)
3	0.94	0.06 (6%)	0.88 (94%)
6	0.92	0.06 (7%)	0.86 (93%)
12	0.90	0.15 (17%)	0.75 (83%)
25	0.88	0.16 (18%)	0.72 (82%)
50	0.86	0.19 (22%)	0.67 (78%)
100	0.87	0.20 (23%)	0.66 (77%)

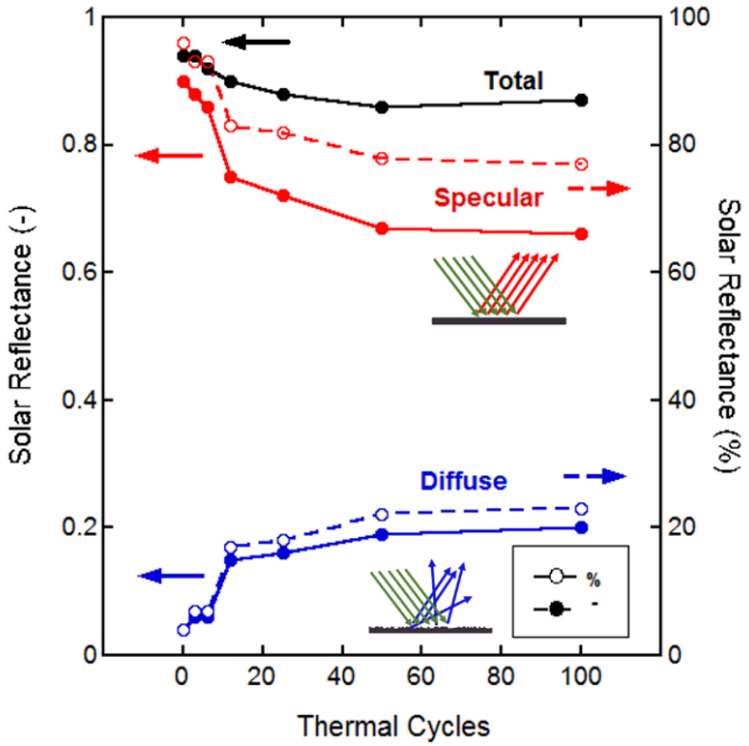

Figure 10: Reflection characteristics of the Ag layer as a function of thermal cycling. Total and diffuse reflectance were measured and used to calculate the amount of specular reflection.

4. Discussion

With increasing thermal cycles, the number of thermal cracks increases, forming a crack network with no preferred crack orientation. Faurie, et al. [40] showed that such a mud-like crack pattern corresponds to equi-biaxial tensile loading of the thin film. During uniaxial tensile straining of the same Ag-Inconel bilayer a two-stage cracking mechanism with primary cracks constrained to the Inconel top layer (crack spacing 2.3 ± 0.2 μm) and secondary cracks penetrating both layers (crack spacing 11.9 ± 1.9 μm) was observed [41]. Due to the small difference in α_{th} between Ag

and Inconel the two metal layers are not acting as individual entities from a thermo-mechanical point of view. Only one type of thermal cracking, namely through thickness cracks through both layers, was observed, governed by the large difference in α_{th} between the metallisation and the polymer substrate. Following the equation $\varepsilon_{th} = \Delta\alpha_{th,\ FEP\text{-}Ag} \bullet \Delta T$, the maximum thermal strain generated within the investigated temperature regime (ΔT = 300 K, $\Delta\alpha_{th,FEP\text{-}Ag}$ = 107 ppm/K, $\alpha_{th,\ Ag}$ = 20 ppm/K [12], $\alpha_{th,\ FEP}$ = 127 ppm/K [11]) is calculated as ε_{th} = 3.2%, exceeding both the fracture strain for primary ($\varepsilon_{f,Inc}$ = 0.25%) and secondary cracking ($\varepsilon_{f,Ag}$ = 1%) in the uniaxial loading case [41]. One should note here, that the thermal expansion coefficient of FEP can be influenced by the processing route and sheet thickness [11] and is highly temperature dependent ($\alpha_{th,\ FEP}$ = 120-170 ppm/K; RT – 160°C [42,43]). Taking into account the temperature dependence of $\alpha_{th,\ FEP}$ the maximum value of thermal strain during cycling is ranging between 3 - 4.5%. This large thermal strain indicates that with one thermal cycle, the film system has fractured. Film fracture is observed in the form of the thermal cracks after 3 cycles, the minimum cycle number investigated in this study. As a results of through thickness cracking, the Inconel can no longer function as a corrosion protection layer. The fact that the system is susceptible to through thickness cracking is particularly important in terms of ground testing, which could then trigger unexpected corrosion effects during ground storage and assembly integration and testing (AIT). The $\Delta\alpha_{th}$ film-substrate is an essential parameter for the thermo-mechanical fragmentation behavior of flexible thin film systems. For Al films on polyimide (Al-PI) ($\Delta\alpha_{th,\ Polyimide\text{-}Al}$ = -12 ppm/K; $\alpha_{th,\ Polyimide}$ = 12 ppm/K [44], $\alpha_{th,\ Al}$ = 24 ppm/K [45]) no thermal cracks were observed under equivalent thermal cycling conditions up to a maximum investigated number of 200 thermal cycles [20]. Due to the small value of $\Delta\alpha_{th}$, the maximum thermal strains are estimated to be only $\varepsilon_{th,Al\text{-}PI}$ = 0.3%. During uniaxial tensile experiments of as-deposited Al-PI, first cracks on the Al surface are visible around 8% strain [46], while in situ electrical resistance measurements detect first signs of non-elastic deformation around 3.2% (failure strain ε_f) [20]. With increasing amount of thermal cycling ε_f is shifted to lower applied strain values.

Despite the formation of thermal cracks, which locally relax the film stresses along the edges, compressive stresses accumulate in the Ag layer as a results of thermal cycling. Figure 11a correlates the evolution of residual stresses in the Ag layer to the observed structural changes (ridges and voids, SEM) and the Ag microstructure (TKD) as a function of thermal cycling. Starting with small tensile residual stresses in the Ag film, the film stresses relax after the first few thermal

cycles and compressive stresses start to build up. At 6 cycles, where first small voids and some ridges are visible by SEM analysis, the Ag layer is almost stress free. After the detection of first voids and ridges compressive stresses start to accumulate in the Ag layer with continued thermal cycling. This can be attributed to the fact that redistribution of material in the Ag layer is constrained by the Inconel overcoat. Between 12 and 25 thermal cycles, significant stress relaxation is observed. At this point, the ridges in the Inconel layer start to crack, thus releasing some of the film's constraint on the Ag film. After 12 cycles, the void size (~150 nm) is of the order of the smaller grains in the initial grain size distribution (Figure 8b, average: 255 ± 136 nm). Between 50 and 100 thermal cycles, the residual film stress increases again as the voids continue to grow in size.

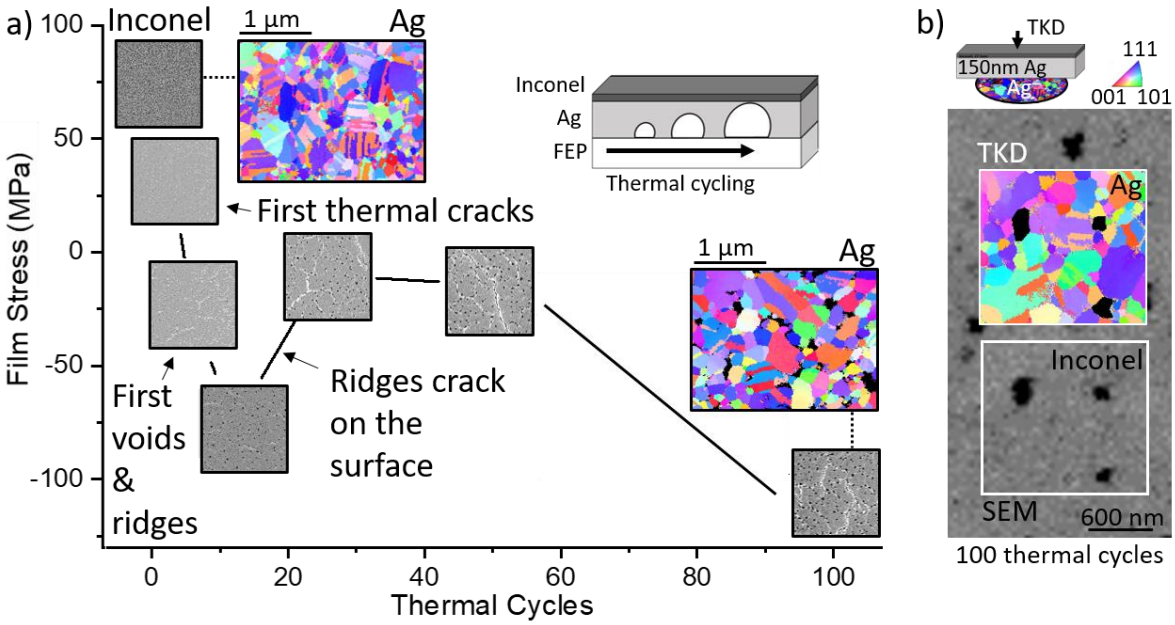

Figure 11: a) Correlation of Ag film stresses, derived from 200 reflections, with the evolution of the surface morphology (SEM) and Ag microstructure (TKD) as a function of thermal cycling. b) Correlation of out of plane TKD map and SEM to investigate void formation in the Ag layer after 100 thermal cycles. In both cases voids appear as black spots.

Stress migration (SM) during thermal cycling potentially causes the formation of voids and ridges. In literature, SM is generally reported as a void and hillock formation mechanism, wherein atoms and vacancies diffuse as a results of local hydrostatic stress gradients in the thin film. Stress gradients, the driving force for diffusion, result from different stress states between the grain

boundaries and the inside of grains when polycrystalline films are subjected to macroscopic uniform stress [18,19]. Considering the thermo-mechanical properties of Ag-FEP, the Ag film is loaded in tension during the heating cycle, where elevated temperatures assist the diffusion process. It is important to note here that annealing experiments at 150°C for 12.5 h, equivalent to the hold time of 50 thermal cycles (± 150°C), did not induce any damage, such as cracks, ridges or voids, in the Ag layer. Therefore, the formation of voids and ridges is clearly related to the changing stress states during thermal cycling. There is no evidence that the overall degradation mechanism observed during thermal cycling in inert N_2 atmosphere would be different from vacuum conditions in space.

An important parameter for the susceptibility of a thin film to SM is the microstructure. Especially the presence of high angle grain boundaries, twin boundaries, and triple points offer easy diffusion paths and assist SM. Sekiguchi, et al. [19] reported void formation at twin interfaces and corners due to stress concentration and diffusion along incoherent twin interfaces in 900 nm electroplated Cu on Ta/SiO_2/Si substrates. Thermal cycling of the Cu films was performed between RT and 450°C. Analysis of the Ag microstructure from TKD maps shows that in the as-deposited state twin boundaries make up approximately 47% of the total length of all grain boundaries (misorientation > 5°), thus providing evidence that the Ag film is prone to SM. After 100 thermal cycles, the amount of twin boundary length was determined as ~48% in the region with voids and ~55% in the region close to the thermal crack, where no voids are present. The different sample preparation methods and resulting TKD scan sizes before and after thermal cycling can influence the grain boundary length values. Despite a similar ratio of twin boundary length in the Ag film before and after thermal cycling, there is a visual difference in the obtained TKD maps (Figure 8a, Figure 11a). While narrow twins are present in the as-deposited state, wider twins are observed after 100 thermal cycles. To quantify the twin width from TKD maps, a parameter δ_{twin} was introduced, which strictly increases with increasing twin width:

$$\delta_{\text{twin}} = \frac{\%A_{twin} * A_{tot}}{L_{twin}} \qquad \text{(Eq. 1)}$$

In Eq. 1 $\%A_{twin}$ equals the area fraction of twinned grains (obtained from OIM analysis software), A_{tot} equals the total scan area and L_{twin} equals the total twin boundary length (also obtained from OIM analysis software). During thermal cycling δ_{twin} increases from δ_{twin} = 0.07 µm in the as-deposited state to 0.12 µm in the region with voids and 0.10 µm in the region close to the thermal

crack (no voids) after 100 thermal cycles. Besides twin widening due to twin boundary migration, the average grain size increases. Largest grains (~700 nm) are observed in the region close to the thermal crack, where no void formation is observed.

Grain growth and twin boundary migration during thermal cycling have been reported in literature for thin films on rigid substrates [47]. Typically, microstructural changes are related to changes in the surface morphology (formation of hillocks, surface roughening) as a results of the changing stress state in the thin film during thermal cycling. Influencing parameters include film thickness, grain size and orientation [13–17]. Hillock formation is one mechanism known to occur in order to relax compressive stresses. Eiper, et al. [17] showed that in Al thin films surface roughening occurred in preference to hillocking below a film thickness of 200 nm. In the case of Inconel-Ag-FEP system, the ridge formation is analogous to the observed surface roughening on rigid substrates to some extent. Also of note is the work of Bigl, et al [14] on 5 µm thick electrodeposited, impurity-free Cu films on Si. During thermal cycling, this film system had a homogenous surface roughness increase and exhibited grain growth with twin boundary migration. Interestingly, no void formation at the interface or along grain boundaries was observed for impurity-free Cu films [14]. Impurity-enrichment (≤ 100 at. ppm) changed the behaviour of Cu towards constrained roughening and severe void formation while exhibiting a stable twin boundary network with no twin boundary migration. In both cases, a small amount of tensile stress accumulated gradually in the Cu films (80 thermal cycles, 170 – 400°C). Main differences of the investigated Inconel-Ag-FEP system compared to literature are the low Ag film thickness, the additional constraint by the thicker Inconel top layer compared to native oxides of Al and Cu and the flexible polymer substrate and resulting Ag-FEP interface.

To investigate microstructural void formation mechanisms, high resolution TKD maps were collected around individual voids. Figure 11b shows a TKD map of the Ag microstructure correlated to the SEM image from the Inconel surface of the same area (15 kV acceleration voltage). As previously mentioned, Ag voids appear as black spots under these SEM imaging conditions. In TKD, voids yield empty scans without Kikuchi lines or Kikuchi patterns with low image quality, as not all holes are completely through thickness after 100 thermal cycles. After filtering the image, removing points with low quality, voids appear as black spots. There is a good correlation between the position and the shape of the voids in the SEM image and the TKD map. Small differences can be due to a slight sample drift during TKD acquisition or due to the fact that

the SE detector captures electrons emitted from the top side of the specimen, while the TKD system captures the electrons emitted from underneath. Rather than being spherical, the voids appear faceted. Void shapes are comparable to those observed during solid state dewetting of thin films [48]. However, annealing temperatures during such experiments are considerably higher compared to this study. In situ solid state dewetting on a bicrystalline 50 nm Al thin film model system (500-550°C) [49] revealed void initiation at surface scratches and to a minor degree within regions without visible surface defects. Other defects such as substrate imperfections at the interface to the films or twin boundaries are also suggested as a starting point for voiding. For pure Au thin films (15-35 nm; 500-900°C) Müller et al. [50] report the nucleation of pores at the film-substrate interface which grow preferably along grain-boundaries and evolve into voids. Consecutive lateral void growth happens via surface diffusion, leading to dewetting of the film. Alloying of Au with a small amount of Pt delayed the onset of dewetting at low temperature. In the current study, the Inconel layer prevents surface diffusion of Ag. While the Ag microstructure contains a lot of the above mentioned potential nucleation sites, no statement about preferred void nucleation and growth directions can be made at this point. However, the presented combined SEM & TKD approach is well-suited to relate thermal-cycling induced subsurface voiding to microstructural aspects in a systematic way in the future.

Due to its chemistry and incoherent structure, the interface between Ag and FEP is the weakest link within the multilayer stack, offering an easy pathway for diffusion of Ag atoms or vacancies, potentially causing the formation of voids. Previous work [15] comparing polycrystalline and epitaxial Al films on Si demonstrated that the epitaxial interface was more stable against dislocation motion, thus hindering surface roughening and microstructural changes. Literature shows that for metal-polymer systems interfacial layers, formed through chemical reactions of metal atoms with the polymer substrates during deposition, are necessary for strong and stable interfaces [21,51,52]. Interface quality is reflected in good mechanical adhesion [20,52] and thermal stability [21]. For vapor deposited Al films on polyimide, very good interfacial adhesion (30.4 ± 6 J/m^2) [46] and resistance against thermal cycling (no void formation) were attributed to a naturally occurring amorphous interlayer [21]. The chemical structure of the FEP does not allow for a chemical reaction between the Ag atoms with the substrate during film deposition, which also makes FEP ideal as a non-stick material [53]. A very low interfacial adhesion energy of about 2 J/m² [46] affirms the assumption of low interface strength for Ag-FEP.

Please see Appendix A for a detailed description of the adhesion energy calculation of the as-deposited system. High resolution analysis of the interface structure with transmission electron microscopy is prohibited by the strong interaction of FEP with an electron beam.

Total solar reflectance values can range from 0 (total absorption of all solar energy) to 1.0 (total reflectance). In the as-deposited state the total reflectance of the Ag layer is 0.94, implying that 94% of the incoming energy is reflected, which is very close to the desired optimum of total reflectance. With increasing number of thermal cycles the total reflectivity decreases due to the formation of thermal cracks and voids in the Ag layer which reduce the ability to reflect back solar energy. The decrease is very rapid up to 25 cycles, at which point a saturation state is reached in which only around 88% of the incoming energy are reflected. The 25 cycles correspond to the turning point in the Ag degradation where the average number of voids reaches a plateau while the existing voids continue to increase in size. Saturation of the total reflectance indicates that void nucleation, which stops after 25 cycles, is dominating the total reflectance behavior. As the decrease in the reflectivity with thermal cycling will cause the spacecraft to heat up, the end of life reflectivity must be considered in equilibrium temperature calculations when designing the thermal control systems. The impact of decreased reflectivity after thermal cycling is similar to that of increased solar absorptance observed in space-retrieved FEP foils due to degradation of the external FEP layer upon space-exposure [9]. The emittance, dominated by the dielectric behavior of the polymer substrate, is likely to remain unaffected [8–10]. The extent of total heat accumulation depends on several factors including the specific space environment, the heat flux from inside the spacecraft and also the view factor to external heat sources.

Void formation in the Ag layer also influences the reflection mode. In the initial state the diffuse reflectance value is measured as 0.04, indicating that about 4% of total reflection happens diffusely, while 96% of the total reflection is specular. With increasing cycle number the amount of diffuse reflection increases up to 23% of the totally reflected energy after 100 cycles ($\rho_D = 0.20$) due to void formation. Saturation of the diffuse/specular ratio is only reached after 50 thermal cycles, indicating that the growth of individual voids after 25 cycles still influences surface roughness and diffuse reflectance. The shift of the saturation regime to higher cycle numbers could also be due to small statistical differences within the measured samples. On spacecraft diffuse reflection can be critical if it is not taken into account in the design. Stray light could, for instance,

enter into optical instruments or start to heat up surfaces, which were originally meant to stay in shadow at all times.

5. Summary

The Inconel-Ag-FEP system, a potential material stack for flexible OSRs in spacecraft, was subjected to thermal cycling to simulate the thermal aspect of the LEO environment. It was found that severe mechanical and optical degradation occurs due to thermal cycling between ± 150°C. The large difference in the coefficients of thermal expansion between the Ag reflecting film and the transparent FEP substrate led to through thickness crack formation after only a few cycles. These cracks were followed by the formation of through thickness voids in the Ag film, initiating at the Ag-FEP interface, and ridges on the Inconel surface to accommodate the voids in the Ag film. The voids reach a saturation density after 25 thermal cycles, but continue to grow with further thermal cycling. The spatial distribution of voids is inhomogeneous, whereby voids only form a certain distance (~ 7 µm) away from a thermal crack. The void sizes are of the order of the smaller grains in the initial Ag grain size distribution and are most likely caused by stress migration of Ag atoms and vacancies. The initial Ag microstructure comprises a high density of twins, known as potential sites for void nucleation. TKD analysis before and after thermal cycling revealed twin widening due to twin boundary migration and grain growth, whereby the largest grains are found close to thermal cracks in regions with no voids. XRD analysis found that a compressive stress builds-up in the Ag film during thermal cycling. As a result of crack and void formation, the reflective properties of the material deteriorate, with decreasing solar reflectance values and increased amounts of diffuse reflection after thermal cycling. Deterioration of the thermo-optical properties would most likely cause the spacecraft to heat up or stray light to reach sensitive optical onboard instruments. In order to mitigate the degradation caused by LEO thermal cycling it is recommended to tailor the material stack with respect to the individual thermal properties (minimized $\Delta\alpha_{th}$) as well as interfacial properties. For example, the addition of interlayers which reduce the thermal strain and/or improve the interface strength could increase the lifetime of flexible OSRs in LEO. Furthermore, optimization of the thin film microstructure should be considered, towards a reduced amount of twinning and enhanced diffusion resistance.

Acknowledgements

This work was supported by the European Space Agency (grant number 4000111838/14/NL/PA) and the EMPAPOSTDOCS-II program, which received funding from the European Union's Horizon 2020 research and innovation program under the Marie Skłodowska-Curie grant agreement number 754364. The authors would like to acknowledge HZB for the allocation of synchrotron radiation beamtime and thankfully acknowledges the financial support by HZB (project 16224035-ST and 17205962-ST-1.1-P).

References

[1] C.F. Struller, P.J. Kelly, N.J. Copeland, Aluminum oxide barrier coatings on polymer films for food packaging applications, Surf. Coat. Technol. (2014) 7–13.

[2] J.A. Rogers, Z. Bao, K. Baldwin, A. Dodabalapur, B. Crone, V.R. Raju, V. Kuck, H. Katz, K. Amundson, J. Ewing, P. Drzaic, Paper-like electronic displays: large-area rubber-stamped plastic sheets of electronics and microencapsulated electrophoretic inks, Proc. Natl. Acad. Sci. U. S. A. 98 (2001) 4835–4840. https://doi.org/10.1073/pnas.091588098.

[3] I. Graz, M. Kaltenbrunner, C. Keplinger, R. Schwödiauer, S. Bauer, S.P. Lacour, S. Wagner, Flexible ferroelectret field-effect transistor for large-area sensor skins and microphones, Appl. Phys. Lett. 89 (2006) 073501. https://doi.org/10.1063/1.2335838.

[4] T. Ichino, S. Sasaki, Y. Hasuda, Development of High-Performance Flexible Optical Solar Reflectors, Electron. Commun. Japan. 69 (1986) 99–107.

[5] K. Sun, C.A. Riedel, Y. Wang, A. Urbani, M. Simeoni, S. Mengali, M. Zalkovskij, B. Bilenberg, C.H. De Groot, O.L. Muskens, Metasurface Optical Solar Reflectors Using AZO Transparent Conducting Oxides for Radiative Cooling of Spacecraft, ACS Photonics. 5 (2018) 495–501. https://doi.org/10.1021/acsphotonics.7b00991.

[6] G. Pippin, E. Normand, S. Woll, Analysis of Ag / FEP Thermal from Control Blanket Performance Multiple Satellites, 2001.

[7] H. Fischer, C.O.A. Semprimoschnig, Durability of polymeric materials in space: Application of scanning thermal microscopy, J. Spacecr. Rockets. 46 (2009) 45–50. https://doi.org/10.2514/1.33362.

[8] J.A. Townsend, P.A. Hansen, J.A. Dever, K.K. de Groh, B.A. Banks, L. Wang, and C. He, Hubble Space Telescope metallized Teflon® FEP thermal control materials: on-orbit degradation and post-retrieval analysis, High Perform. Polym. 11 (1999) 81–99. https://doi.org/10.1088/0954-0083/11/1/007.

[9] M. Moser, C.O.A. Semprimoschnig, M.R.J. Van Eesbeek, R. Pippan, Surface and Bulk Degradation of Teflon® FEP Retrieved from the Hubble Space Telescope Solar Arrays, High Perform. Polym. 20 (2008) 429–446. https://doi.org/10.1177/0954008308089707.

[10] J.A. Dever, K.K. de Groh, B.A. Banks, J.A. Townsend, J.L. Barth, S. Thomson, T. Gregory, W. Savage, Environmental exposure conditions for Teflon ® fluorinated ethylene propylene on the Hubble space telescope, High Perform. Polym. 12 (2000) 125–139.

[11] C.S. Kim, T.L. Smith, An improved method for measuring the thermal coefficient of linear expansion of flexible polymer films, J. Polym. Sci. Part B Polym. Phys. 28 (1990) 2119–2126. https://doi.org/10.1002/polb.1990.090281116.

[12] B.A. Rodgers, I.C. Schoonover, L. Jordan, Silver: Its Properties and Industrial Uses, 1940.

[13] G. Dehm, H. Edongue, T.J. Balk, E. Arzt, M. Metallforschung, Mechanical Size-Effects and Dislocation Dynamics in Cu Thin Films, 9 (2003) 246–247. https://doi.org/10.1017/S1431927603023043.

[14] S. Bigl, S. Wurster, M.J. Cordill, D. Kiener, Advanced characterisation of thermo-mechanical fatigue mechanisms of different copper film systems for wafer metallizations, Thin Solid Films. 612 (2016) 154–164. https://doi.org/10.1016/j.tsf.2016.05.044.

[15] W. Heinz, R. Pippan, G. Dehm, Investigation of the fatigue behavior of Al thin films with different microstructure, Mater. Sci. Eng. A. 527 (2010) 7757–7763. https://doi.org/10.1016/j.msea.2010.08.046.

[16] G.P. Zhang, C.A. Volkert, R. Schwaiger, R. Mönig, O. Kraft, Fatigue and thermal fatigue damage analysis of thin metal films, Microelectron. Reliab. 47 (2007) 2007–2013. https://doi.org/10.1016/j.microrel.2007.04.005.

[17] E. Eiper, J. Keckes, K.J. Martinschitz, I. Zizak, M. Cabié, G. Dehm, Size-independent stresses in Al thin films thermally strained down to −100°C, Acta Mater. 55 (2007) 1941–1946. https://doi.org/10.1016/j.actamat.2006.10.052.

[18] Q. Sun, Y. Lu, X. Xu, F. Huang, C. Tang, Morphological evolution and migration behavior of silver thin films on flexible substrates during thermal cycle testing, Adv. Mech. Eng. 10 (2018) 1–6. https://doi.org/10.1177/1687814018795961.

[19] A. Sekiguchi, J. Koike, S. Kamiya, M. Saka, K. Maruyama, Void formation by thermal stress concentration at twin interfaces in Cu thin films, Appl. Phys. Lett. 79 (2001) 1264–1266. https://doi.org/10.1063/1.1399021.

[20] B. Putz, B. Völker, C. Semprimoschnig, M.J. Cordill, Influence of extreme thermal cycling on metal-polymer interfaces, Microelectron. Eng. 167 (2017) 17–22. https://doi.org/10.1016/j.mee.2016.10.012.

[21] B. Putz, G. Milassin, Y. Butenko, B. Völker, C. Gammer, C. Semprimoschnig, M.J. Cordill, Combined TEM and XPS studies of metal - polymer interfaces for space applications, Surf. Coat. Technol. 332 (2017) 368–375. https://doi.org/10.1016/j.surfcoat.2017.07.079.

[22] M.D. Abràmoff, P.J. Magalhães, S.J. Ram, Image processing with imageJ, Biophotonics Int. 11 (2004) 36–41. https://doi.org/10.1117/1.3589100.

[23] P.W. Trimby, Orientation mapping of nanostructured materials using transmission kikuchi diffraction in the scanning electron microscope, Ultramicroscopy. 120 (2012) 16–24. https://doi.org/doi:10.1016/j.ultramic.2012.06.004.

[24] R.R. Keller, R.H. Geiss, Transmission EBSD from 10 nm domains in a scanning electron microscope, J. Microsc. 245 (2012) 245–251. https://doi.org/10.1111/j.1365-2818.2011.03566.x.

[25] A. Hojabri, F. Hajakbari, M. Moazzen, S. Kadkhodaeia, Effect of thickness on properties of copper thin films growth on glass by DC planar magnetron sputtering, J. Nanostructures. 2 (2012) 107–112. https://doi.org/10.7508/jns.2012.01.013.

[26] H. Khachatryan, S.N. Lee, K.B. Kim, M. Kim, Deposition of al thin film on steel substrate: The role of thickness on crystallization and grain growth, Metals (Basel). 9 (2019). https://doi.org/10.3390/met9010012.

[27] D. Többens, S. Zander, KMC-2 : an X-ray beamline with dedicated di raction and XAS endstations at BESSY II, J. Large-Scale Res. Facil. 2 (2016) 1–6.

[28] L. Spieß, G. Teichert, R. Schwarzer, H. Behnken, C. Genzel, Moderne Röntgenbeugung, Vieweg+Teubner Verlag, 2009.

[29] I.C. Noyan, J.B. Cohen, Residual stress: measurement by diffraction and interpretation, Springer-Verlag, New York, 2013.

[30] H. Wern, N. Koch, T. Maas, Selfconsistent calculation of the x-ray elastic constants of polycrystalline materials for arbitrary crystal symmetry, Mater. Sci. Forum. 404–407 (2002) 127–132.

[31] Inconel Technical Data, (2019). https://www.hightempmetals.com/techdata/hitempInconel625data.php.

[32] M.J. Cordill, D.F. Bahr, N.R. Moody, W.W. Gerberich, Recent Developments in Thin Film Adhesion Measurement, IEEE Trans. Device Mater. Reliab. 4 (2004) 163–168. https://doi.org/10.1016/j.msea.2006.08.027.

[33] Z.Y. Huang, W. Hong, Z. Suo, Nonlinear analyses of wrinkles in a film bonded to a compliant substrate, J. Mech. Phys. Solids. 53 (2005) 2101–2118. https://doi.org/10.1016/j.jmps.2005.03.007.

[34] A.A. Taylor, M.J. Cordill, G. Dehm, On the limits of the interfacial yield model for fragmentation testing of brittle films on polymer substrates, Philos. Mag. 92 (2012) 3363–3380. https://doi.org/10.1080/14786435.2012.723145.

[35] D.C. Agrawal, R. Raj, Measurement of the ultimate shear strength of a metal-ceramic interface, Acta Metall. 37 (1989) 1265–1270. https://doi.org/10.1016/0001-6160(89)90120-X.

[36] A.J. Wilkinson, G. Meaden, D.J. Dingley, High-resolution elastic strain measurement from electron backscatter diffraction patterns : New levels of sensitivity, Ultramicroscopy. 106 (2006) 307–313. https://doi.org/10.1016/j.ultramic.2005.10.001.

[37] F. Ahmed, K. Durst, S. Rosiwal, J. Fandrey, J. Schau, M. Göken, In-situ tensile testing of crystalline diamond coatings using Raman spectroscopy, Surf. Coat. Technol. 204 (2009) 1022–1025. https://doi.org/10.1016/j.surfcoat.2009.04.030.

[38] A. Jain, K. Vijayan, Effect of Thermal Aging on the Crystal Structure Characteristics of Poly(tetre fluoro ethylene), Polym. Eng. Sci. (2007). https://doi.org/10.1002/pen.

[39] Sheldahl, The Red Book, (n.d.) 57.

[40] D. Faurie, F. Zighem, P. Godard, G. Parry, T. Sadat, D. Thiaudière, P.-O. Renault, In situ x-ray diffraction analysis of 2D crack patterning in thin films, Acta Mater. 165 (2019) 177–182. https://doi.org/10.1016/j.actamat.2018.11.040.

[41] B. Putz, C. May-Miller, V. Matl, B. Völker, D.M. Többens, C. Semprimoschnig, M.J. Cordill, Two-stage cracking of metallic bi-layers on polymer substrates under tension, Scr. Mater. 145 (2018) 5–8. https://doi.org/10.1016/j.scriptamat.2017.09.039.

[42] S.H. Jen, S.M. George, R.S. McLean, P.F. Carcia, Alucone interlayers to minimize stress caused by thermal expansion mismatch between Al2O3 films and Teflon substrates, ACS Appl. Mater. Interfaces. 5 (2013) 1165–1173. https://doi.org/10.1021/am303077x.

[43] R.K. Kirby, Thermal expansion of polytetrafluoroethylene (Teflon) from -190 to +300 C, J. Res. Natl. Bur. Stand. (1934). 57 (1956) 91. https://doi.org/10.6028/jres.057.010.

[44] http://www.upilex.jp/en/upilex_grade.html, (2019).

[45] ASM International Handbook Committee, ASM Ready Reference: Thermal Properties of Metals, in: Electron. Prop. Mater., 2011: pp. 439–441. https://doi.org/10.1007/978-1-4419-8164-6_22.

[46] B. Putz, Mechanical and Interfacial Integrity of Metal-Polymer multilayer Systems, PhD Thesis, Univ. Leoben, Leoben, Austria. (2017).

[47] D. Kim, W.D. Nix, R.P. Vinci, M.D. Deal, J.D. Plummer, W.D. Nix, Study of the effect of grain boundary migration on hillock formation in Al thin films, J. Appl. Phys. 90 (2001). https://doi.org/10.1063/1.1381045.

[48] C. V. Thompson, Solid-State Dewetting of Thin Films, Annu. Rev. Mater. Res. 42 (2012) 399–434. https://doi.org/10.1146/annurev-matsci-070511-155048.

[49] S.W. Hieke, M.G. Willinger, Z.J. Wang, G. Richter, D. Chatain, G. Dehm, C. Scheu, On pinning-depinning and microkink-flow in solid state dewetting: Insights by in-situ ESEM on Al thin films, Acta Mater. 165 (2019) 153–163. https://doi.org/10.1016/j.actamat.2018.11.028.

[50] C.M. Müller, R. Spolenak, Dewetting of Au and AuPt alloy films : A dewetting zone model, J. Appl. Phys. 113 (2013) 094301: 1–12. https://doi.org/10.1063/1.4794028.

[51] S.H. Oh, C. Rentenberger, J. Im, C. Motz, D. Kiener, H.P. Karnthaler, G. Dehm, Dislocation plasticity of Al film on polyimide investigated by cross-sectional in situ transmission electron microscopy straining, Scr. Mater. 65 (2011) 456–459. https://doi.org/10.1016/j.scriptamat.2011.06.001.

[52] A.A. Taylor, M.J. Cordill, L. Bowles, J. Schalko, G. Dehm, An elevated temperature study of a Ti adhesion layer on polyimide, Thin Solid Films. 531 (2013) 354–361. https://doi.org/10.1016/j.tsf.2013.01.016.

[53] Ó. Rodr, P.E. Romero, C. Soriano, L. Sevilla, G. Guerrero-vaca, Study on the Main Influencing Factors in the Removal Process of Non-Stick Fluoropolymer Coatings Using Nd : YAG Laser, Polymers (Basel). 123 (2019) 1–14. https://doi.org/10.3390/polym11010123.

[54] M.J. Cordill, F.D. Fischer, F.G. Rammerstorfer, G. Dehm, Adhesion energies of Cr thin films on polyimide determined from buckling: Experiment and model, Acta Mater. 58 (2010) 5520–5531. https://doi.org/10.1016/j.actamat.2010.06.032.

[55] D. Nečas, P. Klapetek, Gwyddion: an open-source software for SPM data analysis, Open Phys. 10 (2012) 181–188.

[56] G. Parry, J. Colin, C. Coupeau, F. Foucher, A. Cimetière, J. Grilhé, A. Cimetiere, J. Grilhe, Effect of substrate compliance on the global unilateral post-buckling of coatings: AFM observations and finite element calculations, Acta Mater. 53 (2005) 441–447. https://doi.org/10.1016/j.actamat.2004.09.039.

[57] W.D. Callister, Materials Science and Engineering: An Introduction, 5th Editio, John Wiley & Sons, Inc., New York, 2000.

[58] G. Fleury, C. Malhaire, C. Populaire, M. Verdier, A. Devos, P.L. Charvet, J.P. Polizzi, Mechanical cross-characterization of sputtered inconel thin films for MEMS applications, Sensors Actuators, B Chem. 126 (2007) 48–51. https://doi.org/10.1016/j.snb.2006.10.038.

[59] V.M. Marx, C. Kirchlechner, I. Zizak, M.J. Cordill, G. Dehm, Adhesion measurement of a buried Cr interlayer on polyimide, Philos. Mag. 95 (2015) 1982–1991. https://doi.org/10.1080/14786435.2014.920543.

[60] A.G. Evans, M. Rühle, B.J. Dalgleish, P.G. Charalambides, The Fracture Energy of Bimaterial Interfaces, Metall. Trans. A. 21A (1990) 2419–2429.

[61] P.S. Ho, Chemistry and adhesion of metal-polymer interfaces, Appl. Surf. Sci. 41–42 (1989) 559–566. https://doi.org/10.1016/0169-4332(89)90122-0.

[62] P.S. Ho, F. Faupel, Adhesion and deformation study of metal/polymer structures by a stretch deformation method, Appl. Phys. Lett. 53 (1988) 1602–1604. https://doi.org/10.1063/1.99924.

[63] P. Phuku, P. Bertrand, Y. De Puydt, Adhesion, microstructure and composition of thermally evaporated aluminium thin layers on polyethylene terephthalate films, Thin Solid Films. 200 (1991) 263–274. https://doi.org/10.1016/0040-6090(91)90198-7.

[64] K.-S. Kim, J. Kim, Elasto-Plastic Analysis of the Peel Test for Thin Film Adhesion, J. Eng. Mater. Technol. 110 (1988) 266–273.

Appendix A: Adhesion energy calculation of the Ag-FEP interface

The adhesion model for tensile induced delamination by Cordill, et al. [54] was used to calculate the adhesion energy of the as-deposited Ag-FEP interface. Buckles formed during uniaxial tensile experiments parallel to the straining direction at around 4% strain were used to evaluate the interface adhesion [41]. Atomic force microscopy (AFM, Veeco Dimension 3100) and the open software GWYDDION [55] were used to measure the buckle dimensions (buckle height, δ and half buckle width, b) from extracted surface profiles. The adhesion model is best applied to the first stages of buckling where symmetric buckle geometries without cracks at the buckle ridge are present. Therefore, a maximum strain of $\varepsilon = 6\%$ was chosen to measure buckle geometries and calculate interfacial adhesion energy. At this early stage of delamination the buckles are distinct enough to unambiguously measure their dimensions. With increasing strain sink-ins started to form around the edges towards the top of the buckle due to the difference in Poisson's ratios (film and substrate) and the induced compressive stress [56]. To ensure the validity of the model and to exclude sink-in effects the half buckle width, b, and buckle height, δ, were measured from AFM images at the tail of each buckle, as shown in Figure A1.

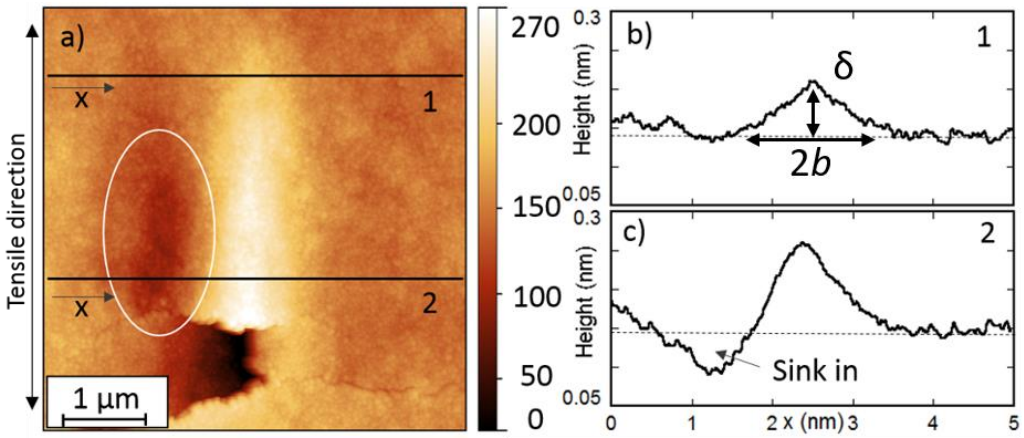

Figure A1: Tensile induced delamination of the as-deposited Inconel-Ag-FEP system. (a) AFM height image of a buckle after 6% strain. Tensile direction is marked with double sided arrow and sink-in area indicated with the white circle. (b) and (c) Extracted surface profiles from (a) with the FEP interface indicated with a dashed line. (b) Profile 1: measured at tail, no sink-in, used for interfacial adhesion. Profile 2: sink-in visible on the left side. [46]

At least 30 measurements were used to calculate the interface adhesion energy. The half buckle width and the buckle height are both normalized by the total film thickness, *h*, and plotted using the following equation [54]:

$$\left(\frac{\delta}{h}\right)^{\frac{1}{2}} = (2\alpha)^{\frac{1}{4}}\left(\frac{b}{h}\right)\left[1+\sqrt{1+\frac{3}{4}\alpha\left(\frac{b}{h}\right)^{4}}\right]^{-\frac{1}{4}}, \qquad \text{(A1)}$$

with α as a fitting parameter for the minimum data measured. Knowing α, the interfacial adhesion energy Γ is calculated using:

$$\Gamma = \frac{\alpha h E'}{4}\left(\frac{\pi}{2}\right)^{4}, \qquad \text{(A2)}$$

where the modified elastic modulus, E′, is calculated as E′=E/ (1−ν2). A detailed description of the model can be found in [54]. Figure A2 summarizes the results of the adhesion measurements for the as-deposited film system.

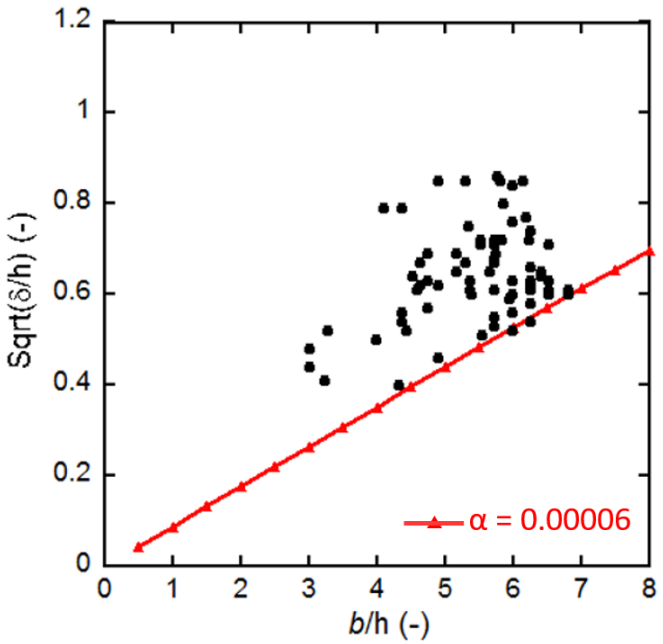

Figure A2: Interfacial adhesion of the Ag-FEP interface.

The red curve in Figure A2 shows Eqn. (A1) with a minimum α value of 6×10^{-5}.With the minimum α value 6×10^{-5} (standard deviation for α: 1×10^{-5}) the interfacial adhesion energy of Ag-FEP was determined as 1.7 ± 0.3 J/m^2 using the total film thickness of 180 nm and a weighted parallel connection of the material constants for Ag (83%, E = 83 GPa, ν = 0.37, [57]) and Inconel (17%, E = 166 GPa, ν = 0.33, [58]). With 150 nm the Ag layer is very strong compared to the influence of the 27.5 nm Inconel layer. For multilayer systems the parallel connection of modulus

and Poisson's ratio (E = 91 GPa and ν = 0.36) was found to describe the buckling condition very well [59]. The calculated adhesion value for the Ag-FEP is at the lower bound of metal-polymer adhesion range found in literature (4 J/m^2 up to 200 J/m^2) [54,60–64], which mainly depends on the reactivity of the metal-polymer pair, parameters during film deposition and the method of measurement. However, it is in good correlation with the relatively low buckling strain of 4%.